

Cosmology with the shear-peak statistics

J. P. Dietrich^{1*} and J. Hartlap²

¹*ESO, Karl-Schwarzschild-Str. 2, 85748 Garching b. München, Germany*

²*Argelander-Institut für Astronomie, Auf dem Hügel 71, 53121 Bonn, Germany*

Accepted 2009 October 23. Received 2009 September 26; in original form 2009 June 16

ABSTRACT

Weak-lensing searches for galaxy clusters are plagued by low completeness and purity, severely limiting their usefulness for constraining cosmological parameters with the cluster mass function. A significant fraction of ‘false positives’ are due to projection of large-scale structure and as such carry information about the matter distribution. We demonstrate that by constructing a “peak function”, in analogy to the cluster mass function, cosmological parameters can be constrained. To this end we carried out a large number of cosmological N -body simulations in the Ω_m - σ_8 plane to study the variation of this peak function. We demonstrate that the peak statistics is able to provide constraints competitive with those obtained from cosmic-shear tomography from the same data set. By taking the full cross-covariance between the peak statistics and cosmic shear into account, we show that the combination of both methods leads to tighter constraints than either method alone can provide.

Key words: cosmological parameters – large-scale structure of Universe – gravitational lensing

1 INTRODUCTION

The number density of clusters of galaxies is a sensitive probe for the total matter density of the Universe Ω_m , the normalisation of the power spectrum σ_8 , and the evolution of the equation of state of the Dark Energy w (e.g., Wang & Steinhardt 1998; Haiman et al. 2001; Weller et al. 2002). For some time it was thought that weak gravitational lensing, which by its nature is sensitive to dark and baryonic matter alike and independent of the dynamical or evolutionary state of the cluster, could be used to construct clean, purely mass selected cluster samples. However, ray-tracing simulations through cosmological N -body simulation made it clear that weak-lensing selected clusters are not at all mass selected but selected by the shear of the projected mass along the line of sight (e.g., Hamana et al. 2004; Hennawi & Spergel 2005; Dietrich et al. 2007). As a result, blind searches for galaxy clusters using weak lensing have both low purity and completeness (e.g., Schirmer et al. 2007; Dietrich et al. 2007).

Gravitational lensing is, due to the large intrinsic ellipticity scatter of background galaxies, an inherently noisy technique. This shape noise is the dominant noise source at the low signal-to-noise ratio (SNR)

end of the weak-lensing selection function, while projections of large-scale structure (LSS) along the line-of-sight (LOS) dominate the noise budget of highly significantly detected peaks (Dietrich et al. 2007). Both sources of noise affect purity and completeness. Galaxy clusters aligned with underdense regions are not visible as significant overdensities, while the projection of uncorrelated overdensities can mimic the shear signal of galaxy clusters. While these effects can be taken into account (Marian & Bernstein 2006), they degrade the constraints on cosmological parameters one can obtain using weak-lensing selected galaxy clusters.

Of course such projected peaks are noise or false positives only in the sense of galaxy cluster searches. They are caused by real structures along the line-of-sight and as such carry information about the matter power spectrum. Whereas analytical models exist for the halo mass function (Press & Schechter 1974; Sheth & Tormen 2002), no such model exists for the number density of peaks in weak lensing surveys. Probably no such prediction can be made analytically because the abundance of peaks depends on projections of uncollapsed yet highly non-linear structures like filaments of the cosmic web. As an additional complication the observed number of peaks depends on observational parameters like limiting magnitude, redshift distribution, and intrinsic ellipticity dispersion.

In the absence of an analytic framework, ray-tracing

* E-mail: jorgd@umich.edu (JPD); hartlap@astro.uni-bonn.de (JH)

through N -body simulations can be used to numerically compute the “peak function” (in analogy to the mass function) for a survey and study its variation with cosmological parameters. Here we present a large set of such simulations aimed at demonstrating the usefulness of the shear-peak statistics for constraining cosmological parameters. We consider this work to be a pilot study and limit ourselves to the variation of the peak function with Ω_m and σ_8 and its ability to break the degeneracy between these two parameters encountered in the 2-point cosmic-shear correlation-function. Unlike Marian et al. (2009) who showed that the projected mass function, which is difficult to measure, scales with cosmology essentially in the same way as the halo mass function, we study the cosmological dependence of the directly observable aperture mass statistics.

2 METHODS

2.1 N -body simulations

We carried out N -body simulations for 158 different flat Λ CDM cosmologies with varying Ω_m , Ω_Λ , and σ_8 . Figure 1 shows the distribution of these simulations in the Ω_m - σ_8 plane. All simulations had 256^3 dark matter particles in a box with $200 h_{70}^{-1}$ Mpc side length. These choices reflect a compromise we had to make between computing a large number of simulations to sample our parameter space on the one hand and to have a fair representation of very massive galaxy clusters dominating the cosmological sensitivity of the halo mass function on the other hand. These simulation parameters were chosen such that we can expect the presence of $10^{15} h_{70}^{-1} M_\odot$ mass halos at redshift $z = 0$ in the simulation box in our choice of fiducial cosmology $\pi_0 = (\Omega_{m0} = 0.27, \Omega_\Lambda = 0.73, \Omega_b = 0.04, \sigma_{80} = 0.78, n_s = 1.0, \Gamma = 0.21, h_{70} = 1)$.

We computed 35 N -body simulations for this fiducial cosmology to estimate the covariance of our observables. The total number of N -body simulations is thus 192. Particle masses depend on the cosmology and range from $m_p = 9.3 \times 10^9 M_\odot$ for $\Omega_m = 0.07$ to $m_p = 8.2 \times 10^{10} M_\odot$ for $\Omega_m = 0.62$. The particle mass at our fiducial cosmology is $m_p = 3.6 \times 10^{10} M_\odot$.

The N -body simulations were carried out with the publicly available TreePM code GADGET-2 (Springel 2005). The initial conditions were generated using the Eisenstein & Hu (1998) transfer function. We started the simulations at $z = 50$ and saved snapshots in Δz intervals corresponding to integer multiples of the box size, such that we have a suitable snapshot for each lens plane of the ray-tracing algorithm. The Plummer-equivalent force softening length was set to $25 h_{70}^{-1}$ kpc comoving. We checked the accuracy of our N -body simulations by comparing their matter power spectra with the fitting formula of Smith et al. (2003). Additionally, we also detected halos using a friend-of-friend halo finder and compared their mass function to that of Jenkins et al. (2001). All tests were done for a number of different cosmologies and redshifts to ensure that the simulations match our expectations over the parameter and redshift range under investigation here.

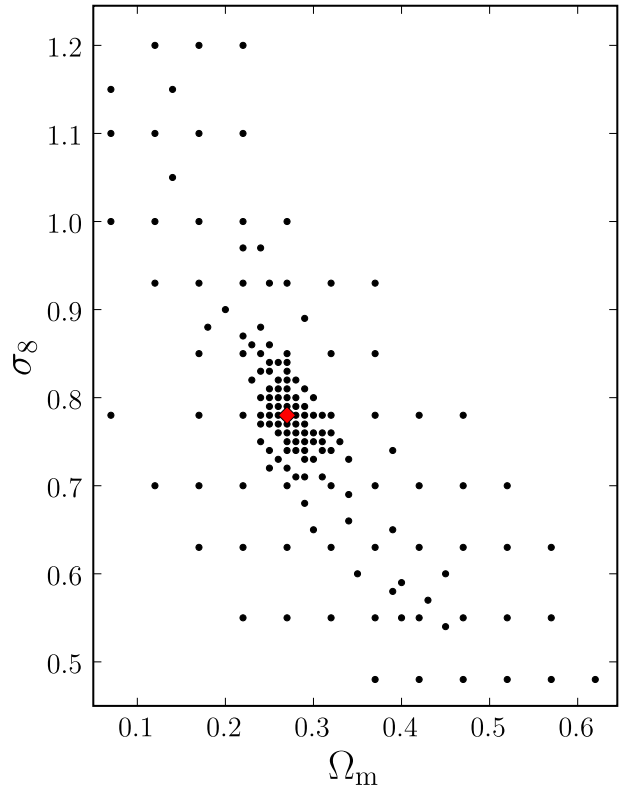


Figure 1. Location of the 158 different cosmologies in the Ω_m - σ_8 plane for which N -body simulations were computed. The red diamond marks the fiducial cosmology at $(\Omega_m, \sigma_8) = (0.27, 0.78)$.

2.2 Ray-tracing

We used the multiple lens-plane algorithm (e.g. Blandford & Narayan 1986; Schneider et al. 1992; Seitz et al. 1994; Jain et al. 2000; Hilbert et al. 2009) to simulate the propagation of light rays through the matter distribution provided by the N -body simulations: for a given N -body simulation, we constructed the matter distribution along the line of sight by tiling snapshots of increasing redshift. The matter distribution of each snapshot was projected onto a lens plane located at the snapshot redshift.

Note that the boxes are just small enough for the cosmic evolution during the light travel time through a box to be negligible. This ensures that the matter distribution does not change significantly in the volume that is represented by a particular lens plane, and that the scale factor and the comoving angular diameter distances to the structure projected onto this plane are essentially the same. If the latter were not the case, this would lead to an erroneous conversion of physical scales on the lens plane to angular scales on the sky. Our allowed us to project a complete snapshot onto one lens plane instead of creating several smaller redshift slices as was done in Hilbert et al. (2009), which reduces the complexity of the ray-tracing considerably.

Since the snapshots basically contain the same matter distribution at slightly different stages of evolution, measures have to be taken to avoid the repetition of struc-

tures along the line of sight. Making use of the periodic boundary conditions of the simulation volume, we applied random rotations, translations, and parity flips to the matter distribution of each snapshot prior to the projection. For the ray-tracing, we assumed that light rays are only deflected at the lens planes and propagate freely in between. We compute the Fourier transform of the deflection potential on each plane from the projected mass density by solving the Poisson equation in Fourier space using FFT, again exploiting the periodic boundary conditions. From this, the Fourier transforms of the deflection angles and their derivatives can be obtained using simple multiplications. Finally, these quantities are transformed to real space using an inverse FFT. More details on the formalism can be found, e.g., in Jain et al. (2000). With this, a set of light rays (forming a grid in the image plane) can be propagated from the observer through the array of lens planes using a recursion formula (see Hilbert et al. 2009). Similarly, the Jacobian matrix of the lens mapping from the observer to each of the lens planes can be obtained.

We then sampled the image plane uniformly with galaxies, the redshift of which was drawn from a distribution of the form

$$p(z) \propto \left(\frac{z}{z_0}\right)^\alpha \exp\left[-\left(\frac{z}{z_0}\right)^\beta\right]. \quad (1)$$

The Jacobian matrices were interpolated from the grid onto the galaxies (in the plane of the sky as well as in redshift) and the reduced shear was computed. We simulated a CFHTLS-Wide like survey for which we created five 6×6 sq. deg. patches from every N -body simulation. The parameters of the redshift distribution (1) were set to $\alpha = 0.836$, $\beta = 3.425$, and $z_0 = 1.171$, as determined for the CFHTLS-Wide (Benjamin et al. 2007). We set the galaxy number-density to $n_g = 25 \text{ arcmin}^{-2}$ and the intrinsic ellipticity dispersion to $\sigma_\varepsilon = 0.38$. Because very few galaxies are present at high redshifts, the redshift distribution was cut off at $z = 3.0$ to save computing time.

2.3 Peak detection

2.3.1 Aperture mass in 2-d

The tidal gravitational field of matter along the line-of-sight causes the shear field $\gamma(\boldsymbol{\theta})$ to be tangentially aligned around projected mass-density peaks. We can use this tangential alignment directly to detect weak-lensing peaks, instead of searching for convergence peaks on maps of reconstructed surface mass-density as it has been done sometimes in weak-lensing cluster searches (e.g., Gavazzi & Soucail 2007; Miyazaki et al. 2007). We define the aperture mass (Schneider 1996) at position $\boldsymbol{\theta}_0$ to be the weighted integral

$$M_{\text{ap}}(\boldsymbol{\theta}_0) = \int_{\text{sup}Q} d^2\vartheta Q(\vartheta) \gamma_t(\boldsymbol{\theta}; \boldsymbol{\theta}_0) \quad (2)$$

over the shear component tangential to the line $\boldsymbol{\theta}_0 - \boldsymbol{\theta}$, $\gamma_t(\boldsymbol{\theta}; \boldsymbol{\theta}_0)$. Here $Q(\vartheta) = Q(|\boldsymbol{\theta}|)$ is a radially symmetric, finite and continuous weighting function with

$\lim_{\vartheta \rightarrow \infty} Q(\vartheta) = 0$. For later convenience we also require Q to be normalised to unit area. If $Q(\vartheta)$ follows the expected shear profile of a mass peak, the aperture mass becomes a matched filter technique for detecting such mass peaks. On data the shear field is sampled by galaxies with ellipticities ε_i . Then M_{ap} can be estimated by the sum over N_g galaxies in the aperture,

$$\hat{M}_{\text{ap}} = \frac{1}{n_g} \sum_{i=1}^{N_g} Q(\vartheta_i) \varepsilon_{it}, \quad (3)$$

where ε_{it} is the tangential ellipticity component of the i -th galaxy, defined in analogy to γ_t above.

The SNR of the aperture mass can be computed directly from the data, making use of the fact $\langle M_{\text{ap}} \rangle \equiv 0$. Then the RMS dispersion is $\sigma_{M_{\text{ap}}} = \sqrt{\langle M_{\text{ap}}^2 \rangle}$, which can be estimated by

$$\hat{\sigma}_{M_{\text{ap}}} = \frac{\sigma_\varepsilon}{\sqrt{2}n_g} \left[\sum_{i=1}^{N_g} Q^2(\vartheta_i) \right]^{1/2}, \quad (4)$$

where we have made use of the fact that

$$\langle \varepsilon_i \varepsilon_j \rangle = \frac{\sigma_\varepsilon^2}{2} \delta_{ij}, \quad (5)$$

with σ_ε being the intrinsic ellipticity dispersion. The estimator for the SNR of the aperture mass is then finally

$$\hat{S}(\boldsymbol{\theta}_0) = \frac{\sqrt{2} \sum_i Q(\vartheta_i) \varepsilon_{it}}{\sqrt{\sum_i Q^2(\vartheta_i) \varepsilon_i^2}}. \quad (6)$$

2.3.2 Tomographic aperture mass

The aperture mass statistics locates convergence peaks only in projection on the sky. Using redshift information on the background galaxies, e.g., from photometric redshifts, one can generalise the 2-dimensional aperture mass to a tomographic measure that is able to deproject structures along the line-of-sight and locate peaks in redshift space (Hennawi & Spergel 2005). The likelihood that a peak at a position $\boldsymbol{\theta}_0$ is at a redshift z_d is given by

$$\ln \mathcal{L}(\boldsymbol{\theta}_0, z_d) = \frac{1}{\sigma_\varepsilon^2} \frac{[\sum_i^{n_z} Z(z_i; z_d) M_{\text{ap}}(\boldsymbol{\theta}_0)]^2}{\sum_i^{n_z} Z^2(z_i; z_d)}, \quad (7)$$

where $Z(z_i; z_d)$ is the redshift weight for a background galaxy in the i th redshift bin,

$$Z(z; z_d) = \frac{D_d D_{\text{ds}}}{D_s} \mathcal{H}(z - z_d), \quad (8)$$

with the Heaviside step function \mathcal{H} . A peak is then located at the 3-d position $(\boldsymbol{\theta}_0, z_d)$ that maximises the likelihood \mathcal{L} . For the purpose of this work 10 equally spaced redshift steps $z_d = 0.1 \dots 1.0$ were used. The background galaxies were put into redshift bins with width $\Delta z = 0.01$ assuming perfect knowledge of their redshifts.

As in Dietrich et al. (2007) we used the weight function proposed by Schirmer et al. (2007)

$$Q_{\text{NFW}}(x; x_c) \propto \frac{1}{1 + e^{6-150x} + e^{-47+50x}} \frac{\tanh(x/x_c)}{x/x_c}, \quad (9)$$

where $x = \vartheta/\vartheta_{\text{max}}$ and x_c is a free parameter, which was fixed to the value of $x_c = 0.15$ determined to be ideal for

the detection of galaxy clusters by Hettterscheidt et al. (2005). Q_{NFW} follows the shear profile of an NFW halo with exponential cut-offs as $x \rightarrow 0$ or $x \rightarrow \infty$.

The absolute scale ϑ_{max} determines the halo radius or mass to which the filter function is tuned. The filter scale chosen for our simulations is 5.6 on the sky, corresponding to a radius of $2h_{70}^{-1}$ Mpc at a redshift of $z = 0.3$. At this redshift the lensing efficiency of our survey is maximal and the chosen radius is adjusted to cluster sizes easily detectable with weak lensing while smoothing over smaller halos. This smoothing also ensures that shot noise from unresolved structures in the N -body simulations does not play a role.

Peaks were detected by connected-component labelling of pixels above a detection threshold. We used the 8 connectivity in 2-d and the 26 connectivity in 3-d, i.e., we consider all pixels that are connected via the sides, edges, or corners of a square or a cube as one structure. Additionally, for tomographic peaks the condition was imposed that peaks must be detected in at least three adjacent redshift bins. This additional requirement is used to filter out detections at very high or low redshifts whose true redshift is outside the tomography cube. Such peaks would pile up in the lowest and highest redshift bin and lead to high additional noise in them. At the same time this filter criterion suppresses the inclusion of peaks caused by increasing shot noise at high redshifts caused by the sharply decreasing number density of background galaxies. Such peaks occur typically in only one or two redshift slices.

2.4 Analysis

For every cosmological model the peak function gives a p -dimensional data vector ζ of observables. We will explore several choices of observables below. The choice of cosmological parameters is denoted by π and the model prediction is $\mathbf{m}(\pi)$. The posterior probability distribution is

$$p(\pi|\zeta) = \frac{p(\zeta|\pi)}{p(\zeta)} p(\pi), \quad (10)$$

where $p(\pi)$ is the prior probability distribution, $p(\zeta|\pi)$ is the likelihood, and $p(\zeta)$ is the evidence. We used a flat prior with cutoffs, i.e., $p(\pi) = 1$ if $\Omega_m \in [0.1 : 0.5]$ and $\sigma_8 \in [0.4 : 1.1]$ and $p(\pi) = 0$ otherwise. The evidence in our case simply is a normalisation of the posterior obtained by integrating the likelihood over the support of the prior.

Assuming that ζ has a Gaussian distribution, the likelihood is

$$p(\zeta|\pi) = \frac{1}{(2\pi)^{d/2} \sqrt{\det \Sigma(\pi)}} \times \exp \left\{ -\frac{1}{2} [\zeta - \mathbf{m}(\pi)]^t \Sigma^{-1}(\pi) [\zeta - \mathbf{m}(\pi)] \right\}, \quad (11)$$

where $\Sigma(\pi)$ is the covariance matrix of the d -dimensional vector ζ . Since our parameter space is covered only by discrete points we will compute ζ by fitting smooth functions to our data vectors or by interpolating across our parameter space. Details will be given in Sect. 3.

We obtained estimates \hat{C} of the covariance matrices for the shear tomography and the peak statistics, as well as their cross-covariance, from the field-to-field variation in the 175 ray-tracing simulations for the fiducial cosmology. As indicated in Eq. (11), the covariance in principle depends on cosmology. Since we do not have a sufficient number of simulations for other cosmological parameters, we set $\Sigma(\pi) = \Sigma(\pi_0)$. Although this is an approximation commonly made, neglecting the cosmology dependence of Σ can have a non-negligible impact on the shape of the posterior likelihood, as has been investigated in Eifler et al. (2008) for the case of cosmic shear. Furthermore, we note that the assumption of a Gaussian likelihood is not necessarily justified (Hartlap et al. 2009; Schneider & Hartlap 2009). These studies suggest that both approximations lead to an over-estimation of the errors on the cosmological parameters, so that our confidence regions are most likely very conservative.

A further issue to keep in mind when estimating a covariance matrix from the data or from simulations is that, although the covariance \hat{C} estimated from the data is an unbiased estimator of the true covariance Σ , the inverse \hat{C}^{-1} is not an unbiased estimator of Σ^{-1} . For n independent simulations an unbiased estimator of the inverse covariance is (Hartlap et al. 2007)

$$\widehat{C^{-1}} = \frac{n-d-2}{n-1} \hat{C}^{-1}, \quad (12)$$

which is what we used when computing Eq. (11). However, the estimated covariance matrix becomes singular if $d > n-1$, which means that the limited number of ray-tracing simulations available to us constrains the number of bins that can be used for the analysis.

3 RESULTS

In analogy to the mass function $N(M, z|\pi)$, the peak function measures the abundance of peaks as a function of convergence and redshift $N(\kappa, z|\pi)$, where for single structures along the line-of-sight the variation of the conversion from κ to M with redshift is given by the kernel (8). Because we detected peaks not in convergence maps but in aperture-mass maps or cubes, the SNR of peaks was used as a proxy for mass.

3.1 Constraints from aperture mass maps

As a first step we show that constraints on $\pi = (\Omega_m, \sigma_8)^t$ can be obtained from the peak statistics in the absence of redshift information. A similar study was recently presented by Wang et al. (2009), who demonstrated that parameters of the Dark Energy equation of state can be constrained from high convergence regions. We detected peaks in aperture-mass SNR maps as described in Sect. 2.4 with a detection threshold of 3.25σ .

Binning the peaks by SNR is not an ideal way to use information about their projected mass since either high SNR bins in cosmologies with low clustering remain empty, or very massive peaks are beyond the SNR of the maximum bin. Instead we used the cumulative SNR distribution of peaks. The function $\mathcal{S}(\Omega_m, \sigma_8) : \mathbb{R}^2 \rightarrow \mathbb{R}^{n_{\text{bin}}}$

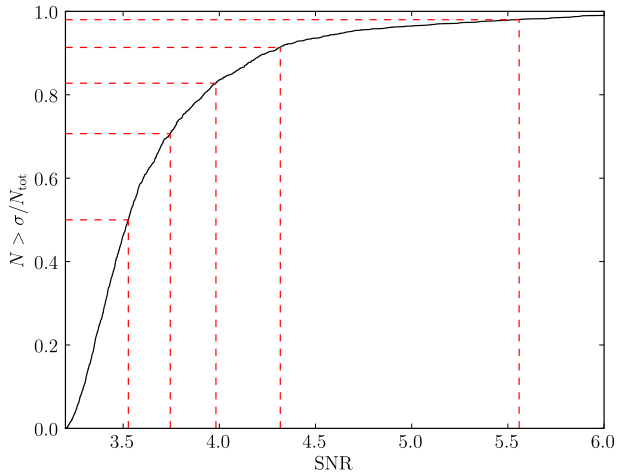


Figure 2. Construction of the function \mathcal{S} . The solid black line is the cumulative SNR distribution of peaks detected in one of our 35 realizations of the fiducial cosmology. The horizontal dashed lines are the logarithmically spaced percentiles from $f_{\min} = 0.5$ to $f_{\max} = 0.98$ at which the cumulative SNR distribution is sampled. The corresponding SNR values denoted by the vertical dashed lines are the values in our data vector.

gives the SNR at which the cumulative distribution exceeds the f th percentile for n_{bin} values of f ranging from f_{\min} to f_{\max} . Figure 2 illustrates how \mathcal{S} is constructed.

We measured $\mathcal{S}(\Omega_m, \sigma_8)$ for $n_{\text{bin}} = 5$ logarithmically spaced values from $f_{\min} = 0.50$ to $f_{\max} = 0.98$. At the fiducial cosmology these percentiles corresponds to SNR values of 3.5σ and 5.7σ , respectively. Typically several hundred peaks per 36 sq. deg. field were detected so that the 98%ile could be reliably measured.

We used bilinear smoothing splines (Dierckx 1993) to interpolate $\mathcal{S}(\Omega_m, \sigma_8)$ on the grid covered by our N -body simulations. In this section splines are a sufficient description of the variation of \mathcal{S} over our parameter space because we only seek to qualitatively demonstrate the ability of the peak statistics to constrain cosmological parameters and to illustrate some of its properties. We will use a more quantitative approach in the following sections.

Figure 3 shows the confidence contours derived from this statistics in the Ω_m - σ_8 plane. They have a shape similar to that seen in constraints derived from cluster cosmology (e.g., Henry et al. 2009) and cosmic shear (Fu et al. 2008, e.g.,) for a CFHTLS like 180 sq. deg. survey. In order to achieve this, we scaled the covariance, which we computed for the individual 36 sq. deg. fields back to the full survey. The similarity of the constraints is of course no surprise since the peak statistics measures the same density fluctuations as clusters of galaxies and cosmic shear.

Although the spline interpolation is mostly illustrative, we defined a figure of merit (FoM), in analogy to the FoM of the Dark Energy Task Force (Albrecht et al. 2006), as the inverse of the area inside the 95% confidence contour. We used this FoM to characterize how the peak statistics changes when parameters entering the function \mathcal{S} are modified. Here in particular we examined the de-

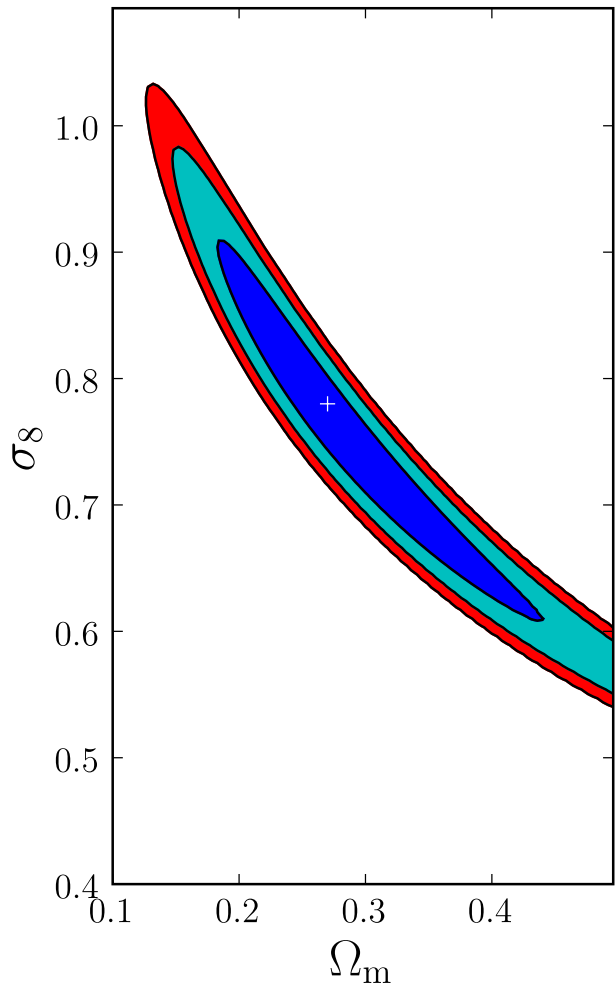


Figure 3. Confidence contours of the aperture mass peak statistics. Shown are the 1-, 2-, and 3σ confidence contours of the \mathcal{S} statistics. The white cross denotes the fiducial cosmology.

pendence of the cosmological constraints on the minimum significance of a detection.

The detection threshold employed in the production of Fig. 3 is very low and a sizable fraction of the peaks detected in this way are simply due to shape noise (Dietrich et al. 2007) and do not carry cosmological information. However, at such a low detection threshold most peaks not caused by noise fluctuations are also not due to a single massive halo but caused by the alignment of LSS along the LOS. We demonstrate that these low significance peaks indeed carry cosmological information by comparing the FoM of the statistics in Fig. 3 to the FoM resulting from the same function \mathcal{S} with a detection threshold of 4.5σ . While the constraints in Fig. 3 correspond to a FoM of 40, the higher detection threshold results in a FoM of only 20. We note that the 95% confidence interval is not fully contained in the support of our flat prior. For the low SNR detection, the 95% confidence interval is cut off by the prior only at the high Ω_m /low σ_8 end. The prior terminates the banana shaped confidence region at both ends for the high SNR detection constraints. Consequently, the true figures of merit

for these statistics are smaller than presented here but more so for the higher detection threshold, making the importance of low SNR peaks even more evident. However, because we used a very simple interpolation scheme, these numbers can only be rough guidelines and we will present a more detailed assessment of the \mathcal{S} function in the next section.

We emphasize that, although there is no reason to believe that the true values of Ω_m or σ_8 are outside the support of our prior, the prior is used only to avoid extrapolating beyond the parameter range covered by the N -body simulations. Since the aim of this study is to examine how well the peak statistics can constrain cosmological parameters, we did not regard the prior as information that should be included in the calculation of the FoM.

3.2 Constraints from peak tomography

In this section we make use of the redshift information in our shear catalogues. We employed the tomographic aperture mass outlined in Sect. 2.3.2 to locate high convergence regions not only in projection on the sky but also along the redshift axis. With 175 independent ray-tracing simulations we could not compute the covariance of the full peak function $\mathcal{N}(S, z)$ for meaningful number of bins in SNR and redshift. Instead, we constructed two separate peak functions from the tomographic data cubes.

The first function measures the abundance of peaks in every redshift bin as a function of cosmology only. We detected peaks as described in Sect. 2.3.2 with a minimum detection threshold of $\sigma_{\min} = 3.2$ and assigned them to a redshift bin based on the redshift z_d that maximises the likelihood (7). With 10 redshift bins, the vector-valued function $\mathcal{M}(\Omega_m, \sigma_8) : \mathbb{R}^2 \rightarrow \mathbb{R}^{10}$ counts the number of peaks in each redshift bin as a function of cosmological parameters. The second function \mathcal{S} uses the SNR information of the detected peaks as defined in the previous section. We used the same values for f_{\min} , f_{\max} , and n_{bin} .

To interpolate $\mathcal{M}(\Omega_m, \sigma_8)$ and $\mathcal{S}(\Omega_m, \sigma_8)$ between points covered by our N -body simulations, we determined fitting functions. These are given in Appendix A and are typically accurate to $\approx 10\%$. Figure 4 shows confidence contours in the Ω_m - σ_8 plane obtained using these fitting functions individually and for the combination of both peak functions, $\zeta_{\mathcal{P}} = (\mathcal{M}, \mathcal{S})^t$. As one would expect from cosmic shear and the cluster mass function, there is a significant degeneracy between Ω_m and σ_8 . The interesting result in Fig. 4 is that \mathcal{M} and \mathcal{S} contain complementary information such that their degeneracies are partly broken. Although the kernel (8) is very broad and the determination of a peak's redshift consequently noisy (see also Hennawi & Spergel 2005) the information on the growth of structure with redshift can be statistically recovered with peak tomography. This then provides information not contained in \mathcal{S} , which is equivalent to a projected mass function. It is important to emphasise that we utilised the full cross-covariance between \mathcal{M} and \mathcal{S} when we computed the joint confidence contours.

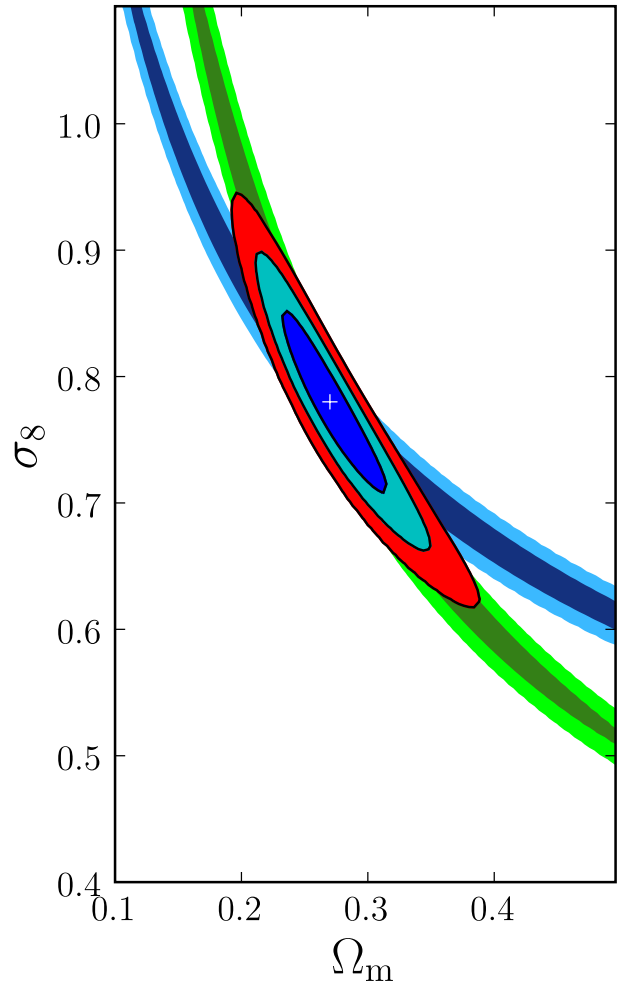


Figure 4. Confidence contours of the peak statistics. Green and blue contours are 1- and 2 σ contours for the \mathcal{M} and \mathcal{S} statistics, respectively. Limited by black contour lines are the joint 1-, 2-, and 3 σ confidence intervals.

We now revisited the issue of how the various parameters of the \mathcal{S} function change the information content of the peak statistics. In the previous section we showed that the detection threshold is an important parameter and that the number of projected low SNR peaks helps to constrain parameters. The same is true for the tomographic peak statistics. The FoM of the \mathcal{S} -function in Fig. 4 is 48. Increasing the detection threshold to 4 σ and keeping all other parameters unchanged decreases the FoM to only 7. Like in the case of the aperture-mass peak statistics, the confidence region is terminated by the prior and the true difference between the different detection thresholds is even larger than suggested by the FoM.

We note that the FoM of the \mathcal{S} function for peak catalogues generated from tomography cubes is not much higher than the rough estimate of the FoM in Sect. 3.1 of the projected peak statistics. The 95% confidence interval in the tomographic case is not fully contained in the parameter space explored by our simulations, whereas, with the spline approximation from the previous section, the low Ω_m /high σ_8 end of the confidence contours is within our parameter range. In any case, the substantial

Table 1. Figures of Merit of different parameters of the \mathcal{S} function.

f_{\min}	f_{\max}	n_{bin}	σ_{\min}	FoM
0.50	0.98	5	3.2	48
0.50	0.98	5	4.0	7
0.08	0.98	10	3.2	48
0.08	0.50	5	3.2	34

gain of the tomographic peak statistics does not come from the deprojection of structures along the LOS but from localising peaks along the redshift axis, i.e., from the combination of the \mathcal{S} and \mathcal{M} statistics.

We also tested several choices of f_{\min} and f_{\max} and the number of bins; Table 1 gives an overview of various settings. Extending f_{\min} to lower values adds almost no information, even if the number of bins is increased to preserve the information in the high SNR bins. For example, decreasing $f_{\min} = 0.08$ and setting $n_{\text{bin}} = 10$ does not improve the FoM. The information content of the \mathcal{S} function is slightly higher with these settings, as is evidenced by a 3% decrease of the area inside the 68% confidence interval. However, the 95% confidence contours within the support of our prior are not tightened.

Despite of this, most of the information is contained in the low SNR regime, as can be seen from the last two rows of Table 1. This information, however, can be recovered with only one or two bins: Figure 2 shows that the low SNR end of the cumulative distribution function has an almost constant slope. This slope is completely determined by the SNR sampled at f_{\min} and the point $(\sigma_{\min}, 0)$, and explains why adding more points at the low end does not increase the FoM. Further information comes only from the shape of the curve in the intermediate SNR range. At the high SNR end the cumulative distribution again has a constant slope and is fully characterized by the last two sample points.

3.3 Combination with cosmic shear

Up to now cosmological information has generally been extracted from lensing surveys via the cosmic-shear two-point correlation functions (2PCF) (e.g., Schneider 2006),

$$\hat{\xi}_{\pm}(\theta) = \langle \epsilon_{\text{t}}(\theta) \epsilon_{\text{t}}(\theta + \vartheta) \rangle \pm \langle \epsilon_{\times}(\theta) \epsilon_{\times}(\theta + \vartheta) \rangle, \quad (13)$$

which are related to the convergence power spectrum \mathcal{P}_{κ} via (e.g., Kaiser 1992)

$$\xi_{+}(\theta) = \int_0^{\infty} \frac{dl}{2\pi} J_0(l\theta) \mathcal{P}_{\kappa}(l) \quad (14)$$

$$\xi_{-}(\theta) = \int_0^{\infty} \frac{dl}{2\pi} J_4(l\theta) \mathcal{P}_{\kappa}(l) \quad (15)$$

Here ϵ_{\times} is the cross-component of the ellipticity and the $J_n(x)$ are the n -th Bessel functions of the first kind. Surveys using this method have led to increasingly tight constraints in the $\Omega_{\text{m}}-\sigma_8$ plane (e.g., Jarvis et al. 2006; Semboloni et al. 2006; Hoekstra et al. 2006; Hettterscheidt et al. 2007; Benjamin et al. 2007; Fu et al. 2008). However, the cosmic shear 2PCF describes the underlying density fluctuations only com-

Table 2. Cosmological constraints using different statistics.

Type	Ω_{m}	σ_8	FoM
Cosmic shear	$0.291^{+0.117}_{-0.091}$	$0.756^{+0.155}_{-0.160}$	71
Peak statistics	$0.273^{+0.063}_{-0.053}$	$0.776^{+0.107}_{-0.096}$	123
Combined	$0.275^{+0.057}_{-0.051}$	$0.774^{+0.095}_{-0.087}$	173

pletely if they are purely Gaussian. Cosmic shear can access information about the non-Gaussianity of the matter distribution only through higher-order correlation functions (see e.g., Takada & Jain 2003, for constraints using the three-point correlation function). The peak statistics on the other hand is most sensitive to extreme overdensities along the LOS, i.e., to those structures that contain most information about non-Gaussianity. It is thus reasonable to assume that both statistics are not completely degenerate and that combining the two does not simply amount to using the same information twice. This expectation is supported by a number of studies looking at the constraints one can place on the Dark Energy equation of state by combining the cluster mass function with other cosmological probes, including weak gravitational lensing (Fang & Haiman 2007; Takada & Bridle 2007; Cunha et al. 2009). Takada & Bridle (2007) in particular examined the full cross-covariance between the cosmic shear 2PCF and cluster counts of shear-selected halos and found that the combination of both methods leads to tighter constraints than either method alone can provide.

Cosmic shear, like the peak statistics, can greatly benefit from the inclusion of redshift information by following the evolution of structure with time (Hu 1999; Bacon et al. 2005). This is done by dividing the galaxy sample into redshift bins and computing their auto- and cross-correlation functions,

$$\hat{\xi}_{\pm}^{(ij)}(\theta) = \langle \epsilon_{\text{t}}^{(i)}(\theta) \epsilon_{\text{t}}^{(j)}(\theta + \vartheta) \rangle \pm \langle \epsilon_{\times}^{(i)}(\theta) \epsilon_{\times}^{(j)}(\theta + \vartheta) \rangle. \quad (16)$$

We used this tomographic 2PCF to compare and combine the constraints obtained from cosmic shear to those from the peak statistics in the same survey.

We split the galaxy catalogue into two redshift bins, separated at redshift $z = 0.6$ and estimated the tomographic cosmic shear 2PCF $\hat{\xi}_{\pm}^{(ij)}$ in our simulation of the fiducial cosmology for 60 logarithmically spaced intervals from $30''$ to 6° . From this we constructed data vectors by averaging the values of 6 consecutive bins into one entry in the data vector, so that we have a 60-dimensional cosmic shear data vector $\zeta_{\text{cs}} = (\hat{\xi}_{+}^{(11)}, \hat{\xi}_{-}^{(11)}, \hat{\xi}_{+}^{(12)}, \hat{\xi}_{-}^{(12)}, \hat{\xi}_{+}^{(22)}, \hat{\xi}_{-}^{(22)})^{\text{t}}$. Using these vectors we computed the covariance of our cosmic shear measurements at the fiducial cosmology. The choice of redshift and spatial bins was motivated by the limited number of independent realisations of our fiducial cosmology, which limits the dimensionality of the data vector.

We predicted the cosmic shear signal on a grid in our parameter space using the transfer function of Eisenstein & Hu (1998) and the non-linear power spectrum of Peacock & Dodds (1996). Figure 5 shows a comparison of constraints obtained using the cosmic shear 2PCF and the he \mathcal{M} and \mathcal{S} peak statistics. The confi-

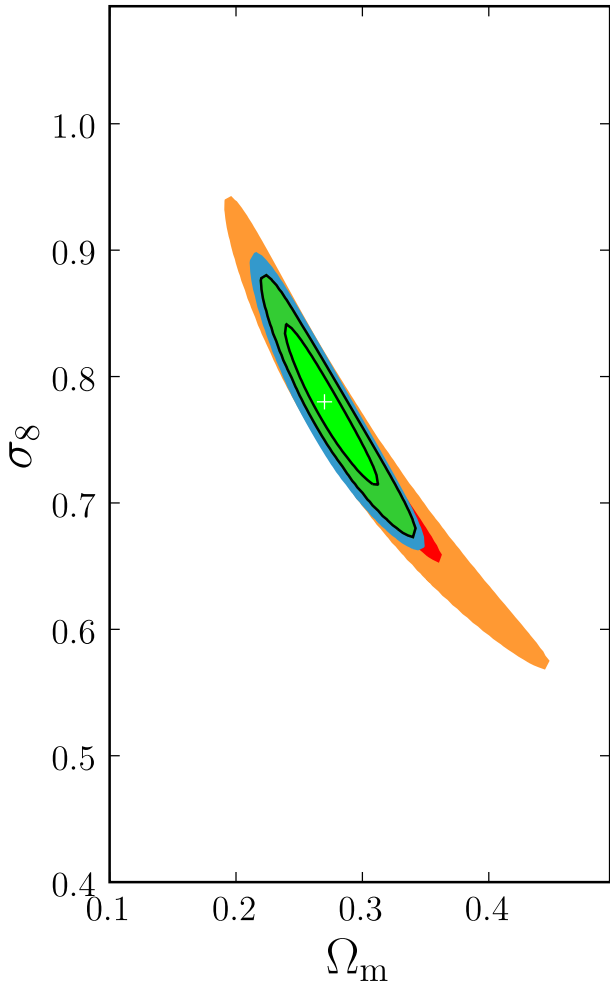


Figure 5. Comparison of the cosmic-shear tomography confidence intervals (orange/red) with the full peak information making use of the combined \mathbf{M} and \mathbf{S} statistics (blue). Shown in green with black outlines is the combination of cosmic-shear and peak statistics. Again, 1- and 2σ intervals are shown in all cases.

dence region of the full peak statistics ζ_p is well aligned with the confidence region of cosmic shear tomography. However, as Table 2 shows, the combined statistics $\zeta = (\zeta_p^t, \hat{\xi}_{cs}^t)^t$ still gives significantly improved constraints; it has a FoM that is about 40% larger than that of cosmic shear tomography alone.

3.4 Stability of the constraints

As mentioned in Sect. 2.4, the estimated inverse covariance becomes singular if $d > n - 1$, and the length of the data vectors is consequently limited by the number of ray-tracing simulations at the fiducial cosmology. The combined statistics vector ζ is 75-dimensional, which is comparable to the number of simulations $n = 175$. Even though we can obtain an unbiased estimate of the inverse covariance, this estimate is potentially very noisy.

We estimate the effect of noise due to the finite number simulations on the constraints derived in the previous section by we creating 1000 bootstrap-like sam-

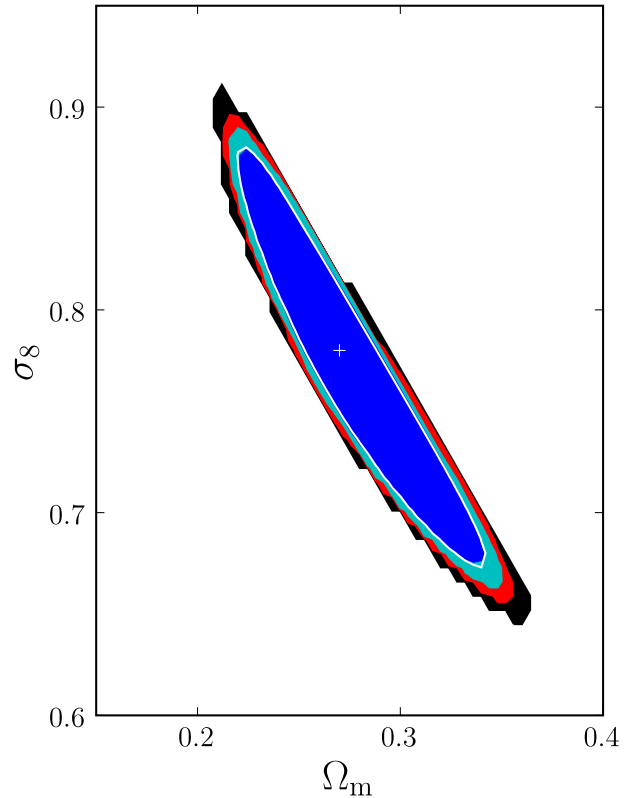


Figure 6. Variation of the constraints when bootstrapping the covariance matrix. The white contour line shows the 95% confidence interval of the combined peak and cosmic shear statistics from Fig. 5. Shaded areas mark the regions inside the bootstrapped 95% confidence interval for x percent of the resamplings, where x is 100 (black), 99 (red), cyan(95), and blue (68).

ples from our set of simulations for the fiducial cosmology. Each sample is constructed by randomly drawing $n = 175$ ray-tracing realisations with replacement. The covariance matrix is estimated for each of the samples. In doing so we kept track how many independent simulations n entered the estimation of the inverse covariance matrix in Eq. (12). At the same time we ensured that we had enough independent simulations to estimate C^{-1} . Finally, we computed the corresponding confidence regions as described before. While not statistically rigorous, this scheme nevertheless illustrates that the confidence intervals are stable with respect to the set of simulations used. Figure 6 shows the variation of the area inside this confidence interval and illustrates that the dependence on the simulations entering the computation of the covariance matrix is small compared to the size of the confidence region.

We have also compared the confidence regions obtained using the fitting functions of Appendix A for the function \mathbf{M} with the constraints computed using the interpolation method described in Section 3.1. While interpolating between simulations for different cosmologies is noisy, the results using the fitting function might be affected by accuracy and choice of the fitting functions. However, we do not find significant differences between the two methods.

4 SUMMARY AND DISCUSSION

We showed in this paper that the number and properties of peaks found in a weak lensing survey can constrain cosmological parameters. This allowed us to turn an important limitation of weak-lensing cluster searches, namely their low purity and completeness, into a source of cosmological information. We note that a similar idea was recently presented by Wang et al. (2009). The most important differences between their and our works are our purely numeric ansatz, the inclusion of tomographic information, and the combination with cosmic shear tomography.

In the pilot study presented here we demonstrated that the peak statistics is able to provide constraints on Ω_m and σ_8 , which are competitive with those obtained from cosmic shear tomography on the same data set. By comparing the constraints obtained from peaks found in maps of aperture mass and tomography cubes we concluded that the tomographic redshift leads to much tighter constraints than working with a 2-dimensional M_{ap} - or convergence map alone. Even though the lensing efficiency varies only slowly with lens redshift and the best estimate of a single peak’s redshift has a large scatter around the true redshift (Hennawi & Spergel 2005), the peak redshift distribution contains valuable information.

By looking at the SNR distribution function we showed that the SNR of peaks, acting as a proxy for mass, also provides information beyond the simple counting of peaks above a detection or mass threshold as it was done by Takada & Bridle (2007) and Fang & Haiman (2007). We showed that peaks with a low SNR, most of which cannot be associated with a single massive halo, contribute significantly to the information content of the peak statistics.

Finally, we investigated how the peak statistics compares with the standard cosmic-shear tomography method and whether a combination of both statistics is useful. We found that the peak statistics gives constraints on Ω_m and σ_8 that are competitive with those expected from a cosmic-shear study on the same survey fields. Taking at face value, our FoM suggests that the peak statistics is indeed the superior method. The comparison, however, is not entirely fair because we used only two redshift bins for the 2PCF tomography while the peak statistics made use of almost perfect redshift information, when we discretized the exact redshifts of the background galaxies into bins of widths $\Delta z = 0.01$. On the other hand, Hennawi & Spergel (2005) found that even with very few redshift bins, the tomographic peak finder is able to locate peaks along the z -axis reasonably well and significantly outperforms a simple M_{ap} peak finder. We thus conclude that the peak statistics gives constraints that are at least comparable to those obtainable from more traditional weak lensing methods.

We combined the peak statistics with the cosmic-shear 2PCF tomography, including the cross-covariance of both statistics measured at our fiducial cosmology. Although both methods have a very similar degeneracy, their combination improves our FoM by about 40%. We surmised that this is due to the inclusion of information about the non-Gaussianity of the matter density field in

the peak statistics, which is not contained in the 2PCF. This result is not unexpected. Takada & Bridle (2007) already found that the combination of cluster counts and shear tomography, including the full covariance, improves cosmological constraints. The new information we add here is that the gain in information continues to be present when cluster counts are replaced with peak counts. The peak statistics, not discriminating between massive halos and chance projections, acts as a “very high-order” cosmic shear method.

Eventually, the much more ambitious question one wants to answer is: *What is the ideal way to extract (lensing) information from present and future cosmological surveys?* We made no attempt to tackle this general problem but showed that a specific higher-order statistics, the peak statistics we introduced in this paper, provides information that can be combined with existing two-point statistics to improve constraints.

A great advantage of our numeric approach to the peak statistics is that observational effects can be included by the simulator to an almost arbitrary degree of precision, given of course these are known and understood. An obvious example would be the inclusion of the holes and gaps in survey fields caused in real data by bright stars, diffraction spikes, ghost images, satellite tracks, and so on.

The disadvantage of this numeric method is its enormous computational cost. The generation of initial conditions, the N -body simulation, ray-tracing, and the tomographic peak finder need about 150 CPUh per simulation on a cluster of Itanium Montecito 1.6 Ghz CPUs. Most of this time is used for the N -body simulation. Since the aperture mass smoothes the convergence field with a kernel of typically 2 Mpc radius high spatial resolution is not required. In this case the computing time can be significantly reduced by replacing the TreePM code with a simple particle-mesh algorithm. But even then, and in the case of massive parallelisation, the wallclock time required to simulate one point in parameter space would prohibit running a standard Markov Chain Monte Carlo method. Population Monte Carlo (PMC, Wraith et al. 2009) allows to investigate sample points independently and thus facilitates the parallelisation beyond the limits of effective interprocess communications of a single simulation.

Another approach to reduce the computation time of Monte Carlo simulations with N -body simulations is the framework proposed by Habib et al. (2007). They developed a mechanism by which the parameter space of interest is optimally sampled with relatively few high-precision simulations. Predictions for untried positions are made from emulations rather than full simulations. An important feature of this method is that the error bounds of the emulations are constrained and that the uncertainties of the emulator output are taken into account in the parameter estimation. Either method, or the combination of PMC with emulators with controlled error, bounds should make the application of the peak statistics to current and future surveys feasible with current high-performance computing hardware. Finally, we point out that the growth of computing power expected

from Moore’s Law is faster than the growth in etendue of envisioned survey facilities.

ACKNOWLEDGEMENTS

This work was supported by AstroGrid-D, a project funded by the Federal Ministry for Education and Research of Germany (BMBF) as part of the D-Grid initiative. This research was in part supported by the DFG cluster of excellence Origin and Structure of the Universe (www.universe-cluster.de). JH acknowledges support by the Deutsche Forschungsgemeinschaft within the Priority Programme 1177 under the project SCHN 342/6, the BMBF through the TR33 “The Dark Universe”, and the Bonn-Cologne Graduate School of Physics and Astronomy. We are very grateful to Torsten Enßlin and Hans-Martin Adorf for their support in getting us onto the grid. We thank Volker Springel for making his initial conditions generator and friend-of-friend halo finder available to us.

REFERENCES

- Albrecht, A., Bernstein, G., Cahn, R., et al. 2006, arXiv:astro-ph/0609591
- Bacon, D. J., Taylor, A. N., Brown, M. L., et al. 2005, MNRAS, 363, 723
- Benjamin, J., Heymans, C., Semboloni, E., et al. 2007, MNRAS, 381, 702
- Blandford, R. & Narayan, R. 1986, ApJ, 310, 568
- Cunha, C., Huterer, D., & Frieman, J. A. 2009, arXiv:0904.1589
- Dierckx, P. 1993, Curve and surface fitting with splines (Oxford University Press)
- Dietrich, J. P., Erben, T., Lamer, G., et al. 2007, A&A, 470, 821
- Eifler, T., Kilbinger, M., & Schneider, P. 2008, A&A, 482, 9
- Eisenstein, D. J. & Hu, W. 1998, ApJ, 496, 605
- Fang, W. & Haiman, Z. 2007, Phys. Rev. D, 75, 043010
- Fu, L., Semboloni, E., Hoekstra, H., et al. 2008, A&A, 479, 9
- Gavazzi, R. & Soucail, G. 2007, A&A, 462, 459
- Habib, S., Heitmann, K., Higdon, D., Nakhleh, C., & Williams, B. 2007, Phys. Rev. D, 76, 083503
- Haiman, Z., Mohr, J. J., & Holder, G. P. 2001, ApJ, 553, 545
- Hamana, T., Takada, M., & Yoshida, N. 2004, MNRAS, 350, 893
- Hartlap, J., Schrabback, T., Simon, P., & Schneider, P. 2009, astro-ph/0901.3269
- Hartlap, J., Simon, P., & Schneider, P. 2007, A&A, 464, 399
- Hennawi, J. F. & Spergel, D. N. 2005, ApJ, 624, 59
- Henry, J. P., Evrard, A. E., Hoekstra, H., Babul, A., & Mahdavi, A. 2009, ApJ, 691, 1307
- Hetterscheidt, M., Erben, T., Schneider, P., et al. 2005, A&A, 442, 43
- Hetterscheidt, M., Simon, P., Schirmer, M., et al. 2007, A&A, 468, 859
- Hilbert, S., Hartlap, J., White, S. D. M., & Schneider, P. 2009, A&A, 499, 31
- Hoekstra, H., Mellier, Y., van Waerbeke, L., et al. 2006, ApJ, 647, 116
- Hu, W. 1999, ApJ, 522, L21
- Jain, B., Seljak, U., & White, S. 2000, ApJ, 530, 547
- Jarvis, M., Jain, B., Bernstein, G., & Dolney, D. 2006, ApJ, 644, 71
- Jenkins, A., Frenk, C. S., White, S. D. M., et al. 2001, MNRAS, 321, 372
- Kaiser, N. 1992, ApJ, 388, 272
- Marian, L. & Bernstein, G. M. 2006, Phys. Rev. D, 73, 123525
- Marian, L., Smith, R. E., & Bernstein, G. M. 2009, ApJ, 698, L33
- Miyazaki, S., Hamana, T., Ellis, R. S., et al. 2007, ApJ, 669, 714
- Peacock, J. A. & Dodds, S. J. 1996, MNRAS, 280, L19
- Press, W. H. & Schechter, P. 1974, ApJ, 187, 425
- Schirmer, M., Erben, T., Hetterscheidt, M., & Schneider, P. 2007, A&A, 462, 875
- Schneider, P. 1996, MNRAS, 283, 837
- Schneider, P. 2006, in Saas Fee Advanced Course 33: Gravitational Lensing: Strong, Weak and Micro, ed. P. Schneider, C. Kochanek, & J. Wambsganss
- Schneider, P., Ehlers, J., & Falco, E. E. 1992, Gravitational Lenses (Gravitational Lenses, XIV, 560 pp. 112 figs.. Springer-Verlag Berlin Heidelberg New York. Also Astronomy and Astrophysics Library)
- Schneider, P. & Hartlap, J. 2009, astro-ph/0905.0577
- Schneider, P., van Waerbeke, L., Jain, B., & Kruse, G. 1998, MNRAS, 296, 873
- Seitz, S., Schneider, P., & Ehlers, J. 1994, Classical and Quantum Gravity, 11, 2345
- Semboloni, E., Mellier, Y., van Waerbeke, L., et al. 2006, A&A, 452, 51
- Sheth, R. K. & Tormen, G. 2002, MNRAS, 329, 61
- Smith, R. E., Peacock, J. A., Jenkins, A., et al. 2003, MNRAS, 341, 1311
- Springel, V. 2005, MNRAS, 364, 1105
- Takada, M. & Bridle, S. 2007, New Journal of Physics, 9, 446
- Takada, M. & Jain, B. 2003, MNRAS, 340, 580
- Wang, L. & Steinhardt, P. J. 1998, ApJ, 508, 483
- Wang, S., Haiman, Z., & May, M. 2009, ApJ, 691, 547
- Weller, J., Battye, R. A., & Kneissl, R. 2002, Physical Review Letters, 88, 231301
- Wraith, D., Kilbinger, M., Benabed, K., et al. 2009, arXiv:0903.0837

APPENDIX A: FITTING FUNCTIONS FOR TOMOGRAPHIC PEAKS

We find that each component of $M(\Omega_m, \sigma_8)$ is well described by the function

$$M_z(\Omega_m, \sigma_8) = Ag(z) [1 + (1+z)^3] \Omega_m^\beta \sigma_8^\alpha P(z, \Omega_m, \sigma_8) + p_3(\Omega_m, \sigma_8) \quad (\text{A1})$$

where $g(z)$ is the distance ratio D_{ds}/D_s averaged over the source redshift distribution (Schneider et al. 1998). The functions P and p_3 are polynomials, where

$$\begin{aligned} p_1 &= p_{10} + p_{11}\Delta\Omega_m + p_{12}\Delta\sigma_8 \\ p_2 &= p_{20} + p_{21}\Delta\Omega_m + p_{22}\Delta\sigma_8 \\ p_3 &= p_{30} + p_{31}\Delta\Omega_m + p_{32}\Delta\sigma_8 \\ P &= 1 + z(p_1 + zp_2), \end{aligned} \quad (\text{A2})$$

with $\Delta\Omega_m = \Omega_m - \Omega_{m_0}$, $\Delta\sigma_8 = \sigma_8 - \sigma_{8_0}$. The constant A , the polynomial coefficients p_{mn} , and the exponents α and β are the free parameters of the fitting function, which are fitted simultaneously for all redshift bins and cosmological parameters. The values of the fit parameters depend on the choice of the signal-to-noise-cut, the ellipticity dispersion, the redshift distribution of the galaxies, the filter function and radius and the galaxy number density. Quoting the best-fit values for our specific choices of these parameters would therefore be of very limited use.

The SNR probability distribution $p(S; \Omega_m, \sigma_8)$ is well described by a log-normal distribution for $x = \log(S^2/10)$

$$\begin{aligned} p(x; \Omega_m, \sigma_8) &= \frac{1}{\sqrt{2\pi x} S \sigma(\Omega_m, \sigma_8)} \times \\ &\exp\left\{-\frac{[\log(x) - \mu(\Omega_m, \sigma_8)]^2}{2\sigma^2(\Omega_m, \sigma_8)}\right\}, \end{aligned} \quad (\text{A3})$$

where the cosmological dependence of μ and σ are described by (double) power laws

$$\begin{aligned} \mu(\Omega_m, \sigma_8) &= A_1 \Omega_m^{a_1} \sigma_8^{b_1} + \Omega_m^{c_1} \sigma_8^{d_1} \\ \sigma(\Omega_m, \sigma_8) &= A_2 \Omega_m^{a_2} \sigma_8^{b_2}. \end{aligned} \quad (\text{A4})$$

The cosmology dependent number count of peaks is given by

$$N(\Omega_m, \sigma_8) = A_3 \Omega_m^{a_3} \sigma_8^{b_3} + \Omega_m^{c_3} \sigma_8^{d_3}. \quad (\text{A5})$$

Note that we do not fit the probability density function (A3) to the data, but the cumulative distribution function which we compute numerically.